Pt single atom captured by oxygen vacancy-rich NiCo layered double hydroxides for coupling hydrogen evolution with selective oxidation of glycerol to formate

Hongjie Yu, Wenxin Wang, Qiqi Mao, Kai Deng, Ziqiang Wang [*], You Xu, Xiaonian Li, Hongjing Wang [*], Liang Wang [*]

State Key Laboratory Breeding Base of Green-Chemical Synthesis Technology, College of 'Chemical Engineering, Zhejiang University of Technology, Hangzhou 310014, PR China

ARTICLE INFO

ABSTRACT

By combining hydrogen evolution reaction (HER) with glycerol oxidation reaction (GOR), high-value chemicals can be obtained at the anode while saving energy to produce hydrogen. Herein, we synthesized Pt_{SA}-NiCo LDHs/NF by anchoring oxygen vacancies in NiCo LDHs with Pt to form $Pt-O_5$ coordination. Density functional theory (DFT) revealed that Pt_{SA} reduced the *d*-band center and optimized ΔG_{H^*}. During HER, LDHs act as active sites to catalyze H-OH cleavage and promote the dissociation of H_2O, while Pt single atoms act as the binding sites for H intermediates, and Pt-O bonds accelerate proton-electron coupling and promote the release of H_2 molecules. In HER//GOR, a cell voltage of only 1.37 V is required to provide a current density of 100 mA cm^{-2} and to produce formate at the anode. This work enables energy-saving hydrogen production and high-value chemicals at the anode, a novel green electrocatalytic synthesis strategy with synergistic coupling and dual promotion.

1. Introduction

Hydrogen is a promising energy carrier with the advantages of high energy density (142 MJ kg^{-1}), high calorific value, sustainability, and cleanness [1–4]. Hydrogen evolution reaction (HER) driven by renewable electricity is an attractive method for zero-emission hydrogen production [5–8]. Although significant progress has been made in the application of non-noble metal catalysts in HER [9–11], platinum remains the most desirable catalyst for HER due to its excellent hydrogen bonding ability [12–14]. Unfortunately, the scarcity and high cost of platinum limit its large-scale application. Therefore, reducing the content of platinum, increasing the number of active sites, lowering the energy barrier, and improving the stability of the catalysts are the key issues to constructing efficient HER catalysts.

Compared with nanoparticle catalysts, single-atom catalysts (SACs) can maximize the dispersion of metal elements [15–18]. While reducing the metal content, they improve the atomic utilization and show the best intrinsic activity of each metal atom [19,20]. In addition, SACs possess abundant unsaturated coordination configurations, unique quantum size effects, and strong metal-carrier interactions [21,22]. Due to these

properties, SACs have a wide range of applications in catalysis and energy conversion [23]. Substituting or anchoring metal atoms on host materials is one way to construct SACs [24,25]. Layered double hydroxides (LDHs) are good host materials for confining single metal atoms due to their high specific surface area and abundant defect sites [26,27]. Nickel-based LDHs are one of the easiest LDHs to prepare. Among them, NiCo LDHs have the advantages of low synthesis cost, high charge storage capacity, large specific surface area, high catalytic activity, and good stability [28]. By regulating the composition, surface environment, defects, and other structural factors of NiCo LDHs, we can improve the nanostructured charge transfer ability of NiCo LDHs and achieve excellent catalytic performance. After anchoring a single atom at the defect site, electron transfer and orbital hybridization occur at the metal-carrier interface to form a new bond. In LDHs, the O atom will bond with the noble metal single atom to form an M-O bond [29], and the *d* electron state of the noble metal will be regulated to enhance the chemisorption and activation of the reaction species, thus reducing the energy barrier and promoting the catalytic performance. Research reported that Pt is mainly an electronic acquisition center when Pt is binding with O, and the O atom acts as the proton capture center [30].

With the production of electrons and protons during HER, the Pt-O bond accelerates proton-electron coupling, which will facilitate the rapid release of H_2 from the Pt-O bond [31]. Besides, in a combination of Pt single atoms and LDHs, LDHs act as the active site for catalyzing H-OH cleavage to promote H_2O dissociation, while Pt single atom acts as the binding site for H intermediate to facilitate H_2 molecule formation [32]. Therefore, it is desirable to construct efficient HER catalysts by anchoring Pt single atoms with oxygen vacancies in LDHs.

The construction of efficient HER and oxygen evolution reaction (OER) catalysts is an important means to reduce the cost of water electrolysis. However, due to the slow intrinsic kinetic process and high theoretical potential (1.23 V vs. RHE), OER consumes nearly 90% of the electric energy in the water electrolysis process and produces low economic benefits of O_2 [33–35]. Recently, some studies have established hybrid water electrolysis systems to replace OER with thermodynamically favorable anodic small molecule oxidation reactions [36–39] (e.g., glycerol oxidation [40–42], methanol oxidation [43,44], and 5-hydroxymethylfurfural oxidation [45,46]). This system can significantly reduce the anodic oxidation overpotential to achieve energy-saving hydrogen production and obtain high-value chemicals at the anode, a new green electrocatalytic synthesis strategy with synergistic coupling and double promotion. However, most of the above small molecule oxidation reactions involve complex oxidation processes with many kinds of products. [47] Therefore, the implementation of small molecule oxidation reactions assists in hydrogen production remains challenging.

In this work, NiCo LDHs act as the host materials to capture Pt single atoms by oxygen vacancies to construct the Pt_{SA}-NiCo LDHs/NF. X-ray absorption spectra (XAS) show that O atoms act as anchor sites to combine with Pt single atoms to form Pt-O_5 coordination and generate strong metal-carrier interactions. The as-obtained Pt_{SA}-NiCo LDHs/NF both served as the anode and cathode electrodes in a hybrid water electrolysis system by coupling hydrogen evolution with selective oxidation of glycerol. The HER//GOR hybrid water electrolysis system requires only a cell voltage of 1.37 V to provide a current density of 100 mA cm^{-2} in an electrolyte of 1 M KOH with 0.1 M glycerol and achieves selective oxidation of glycerol to formate at the anode. Density functional theory (DFT) reveals the d-band center of Pt_{SA}-NiCo LDH/NF is far from the Fermi energy level than that of NiCo LDH/NF. In addition, the HER kinetics of Pt_{SA}-NiCo LDH/NF are fully optimized as the H* coverage increases from 1 to 2. This work establishes an efficient bifunctional catalyst for hydrogen evolution and selective oxidation of glycerol to formate and provides a new idea for energy-saving hydrogen production.

2. Experimental section

2.1. Materials and chemicals

Nickel (II) nitrate hexahydrate (Ni(NO$_3$)$_2$·6 H$_2$O), cobalt (II) nitrate hexahydrate (Co(NO$_3$)$_2$·6 H$_2$O), nickel (II) acetate tetrahydrate (Ni(CH$_3$COO)$_2$·4 H$_2$O), cobalt (II) acetate tetrahydrate (Co(CH$_3$COO)$_2$·4 H$_2$O), potassium hydroxide (KOH) and glycerol were purchased from Aladdin. Potassium tetrachloroplatinate (K$_2$PtCl$_4$) was purchased from Sigma-Aldrich. Commercial Pt/C (20 wt%) was ordered from Alfa Aesar.

2.2. Synthesis of Pt single atom captured by oxygen vacancy-rich NiCo layered double hydroxides on Ni foam (Pt$_{SA}$-NiCo LDH/NF)

Pt single atom captured by oxygen vacancy-rich NiCo layered double hydroxides on Ni foam (Pt$_{SA}$-NiCo LDH/NF) were synthesized by the electrochemical-deposition process, in which pre-treated Ni foam (1 cm × 3 cm) was worked as the working electrode, Ag/AgCl as the reference electrode and platinum sheet as the counter electrode. A mixed precursor solution containing 1.5 mmol Ni(NO$_3$)$_2$·6 H$_2$O, 1.5 mmol Ni(CH$_3$COO)$_2$·4 H$_2$O, 1.5 mmol Co(NO$_3$)$_2$·6 H$_2$O, and 1.5 mmol Co(CH$_3$COO)$_2$·4 H$_2$O, 3 mL K$_2$PtCl$_4$ (20 mM) and 27 mL deionized water

were stirred continuously for 30 min before use. Pt$_{SA}$-NiCo LDH/NF was gained by electrodeposition at a constant potential of − 1.0 V for 1500 s and keeping the electrodeposition areas of 1 cm × 2 cm. The resultant Pt$_{SA}$-NiCo LDH/NF was washed with ethanol and deionized water and dried at 50 ℃ for further use. NiCo LDH/NF was synthesized using the same method without adding K$_2$PtCl$_4$.

2.3. Materials Characterization

The microscopic morphology of the catalysts was investigated by scanning electron microscopy (SEM, ZEISS Gemini SEM 500) with an accelerating voltage of 10 kV. Transmission electron microscope (TEM), high-resolution TEM (HRTEM), and aberration-corrected high-angle annular dark-field scanning TEM (AC-HAADF-STEM) were carried out FEI Thermo Scientific Themis Z instrument equipped with an energy dispersive X-ray spectroscopy (EDX) system. The X-ray diffraction (XRD) patterns were conducted by PANalytical X'Pert Pro MPD with the 2θ range from 10° to 90° and a scan rate of 5°/min. The X-ray photoelectron spectroscopy (XPS) spectra were recorded on Thermo ESCALAB 250XI. The chemical composition was recorded on inductively coupled plasma mass spectrometry (ICP-MS) using a PerkinElmer ICP 2100. The concentration of oxygen vacancies was recorded on the electron paramagnetic resonance (EPR) spectrum (Bruker EMXplus). The X-ray absorption spectra (XAS) including X-ray absorption near-edge structure (XANES) and extended X-ray absorption fine structure (EXAFS) of the catalysts were collected at the SPring-8 14b2, where a pair of channel-cut Si (111) crystals was used in the monochromator. The storage ring was working at the energy of 8.0 GeV with an average electron current of 99.5 mA.

2.4. Electrochemical Measurements

The electrochemical performance measurements were divided into a cathodic hydrogen evolution reaction, an anodic glycerol selective oxidation reaction, and a coupling reaction of HER and GOR. The performance of two half-reactions was investigated in a conventional three-electrode cell system using a CHI 660E electrochemical workstation. In the electrochemical measurements, Pt$_{SA}$-NiCo LDH/NF was the working electrode, carbon rod was the counter electrode, and Hg/HgO was the reference electrode. In addition, HER was measured in 1.0 M KOH. GOR and HER//GOR were measured in 1.0 M KOH with 0.1 M glycerol. The sweep rate for the linear sweep voltammetry (LSV) tests involved in the paper was 5 mV/s, and if not specifically mentioned all LSV curves were iR corrected (95%) to compensate for the electrolyte resistance. The electrochemical impedance spectroscopy (EIS) measurement was conducted in a frequency range of 0.1-100 kHz. Furthermore, the performance of HER//GOR was investigated in a two-electrode cell system by using Pt$_{SA}$-NiCo LDH/NF as both cathode and anode electrodes.

2.5. DFT Calculations

All density functional theory (DFT) calculations were performed using the Vienna Ab initio Simulation Package (VASP) in the context of the generalized gradient approximation (GGA) using the Perdew-Burke-Ernzerhof (PBE) functional in the spin-polarization frame. The projected augmented wave (PAW) potential was chosen to describe the ion nuclei and the valence electrons were taken into account using a plane wave basis set with a kinetic energy cutoff of 450 eV. The DFT-D3 empirical correction method was used to describe van der Waals interactions. Geometry optimizations were performed with the force convergence less than 0.05 eV/Å. All calculations used 2 × 2 × 1 Monkhorst-Pack k-points. All the atoms are relaxed in all the calculations. To overcome this shortcoming, we used the GGA+U method with U-J = 3.32 and 6.2 eV for Co atoms and Ni atoms, respectively. The free energy changes (ΔG) of each elementary reaction step during HER were calculated using the computational hydrogen electrode (CHE) model. In this model, the

chemical potential is equal to the energy of half of the gas-phase H_2 at 0 V vs reversible hydrogen electrode (RHE). The electrode potential, U verse RHE, is taken into consideration by adding-eU when an electron transforming step occurs. That is G(U) = G(0 V) -neU, where n is the number of proton-electron pairs transferred, e is the elementary charge of an electron, and U is the applied potential. The Gibbs free energy was calculated by the following equation:

$$\Delta G = \Delta E + \Delta E_{ZPE} - T\Delta S$$

The value of ΔE, ΔE_{ZPE}, and ΔS denotes the changes in DFT energy, the zero-point energy, and the entropy at 300 K, respectively.

3. Results and discussion

3.1. Catalyst characterizations

As shown in Fig. 1a, Pt single atoms were captured by oxygen vacancy-enriched NiCo layered double hydroxides on Ni foam (Pt_SA-NiCo LDH/NF) through the electrochemical deposition process. During the electrodeposition process, a large number of oxygen vacancies were generated in NiCo LDH/NF due to the addition of Pt precursors that change the deposition rate. These oxygen vacancies will then interact with the Pt precursor ($[PtCl_4]^{2-}$) and the Pt cation breaks with Cl anion to form a stable Pt-O structure with O. Scanning electron microscopy (SEM) images (Fig. S1a and Fig. S1b) and transmission electron microscope (TEM) image (Fig. 1b) show that Pt_SA-NiCo LDH/NF exhibits a two-dimensional (2D) nanosheet array structure. By comparing the SEM images of Pt_SA-NiCo LDH/NF and NiCo LDH/NF, it could be found that the morphology of Pt_SA-NiCo LDH/NF was not much different from that

of NiCo LDH/NF after the introduction of 0.69% atomic ratio of Pt (Fig. S1 and Fig. S2). The formation of Pt nanoparticles was not observed in the TEM images, even though Pt was loaded up to 5.64 wt% as measured by inductively coupled plasma mass spectrometry (ICP-MS) measurement. To further explore the existing state of Pt, this sample was performed by aberration-corrected high-angle annular dark-field scanning TEM (HAADF-STEM). Numerous bright dots were observed from the aberration-corrected HAADF-STEM images and are highlighted by yellow circles (Fig. 1c and d), corresponding to Pt single atoms. A wider range aberration-corrected HAADF-STEM image was shown in Figure S3. Energy dispersive X-ray spectroscopy (EDX) elemental mapping analysis (Fig. 1e) shows a uniform distribution of Ni, Co, O, and Pt elements on Pt_SA-NiCo LDH/NF. These results showed that NiCo LDH/NF can capture Pt ions and form stable Pt single atoms upon the addition of a certain amount of Pt precursors.

Furthermore, the crystal structure of Pt_SA-NiCo LDH/NF was confirmed by an X-ray diffractometer (XRD). As shown in Fig. S4, the diffraction peaks of NiCo LDH/NF correspond to the (003), (006), (012), (018), and (110) planes of the NiCo layered double hydroxides phase (JCPDS No. 40–0216), respectively [48,49]. Besides, compared to the NiCo LDH/NF, the introduction of Pt species did not result in additional diffraction peaks detected in the XRD pattern of Pt_SA-NiCo LDH/NF. However, it can be observed the Pt 4 f spectra of Pt_SA-NiCo LDH/NF (Fig. S5). To some extent, this also proves that Pt species exist as single atoms. Then, the chemical state of Pt_SA-NiCo LDH/NF and NiCo LDH/NF was investigated by X-ray photoelectron spectroscopy (XPS). For Pt_SA--NiCo LDH/NF, the binding energies of Ni $2p_{1/2}$ and Ni $2p_{3/2}$ located at 855.5 and 873.2 eV were assigned to Ni^{2+}, accompanied by two prominent shakeup satellite peaks (861.4 and 879.5 eV) (Fig. 2a) [50,51].
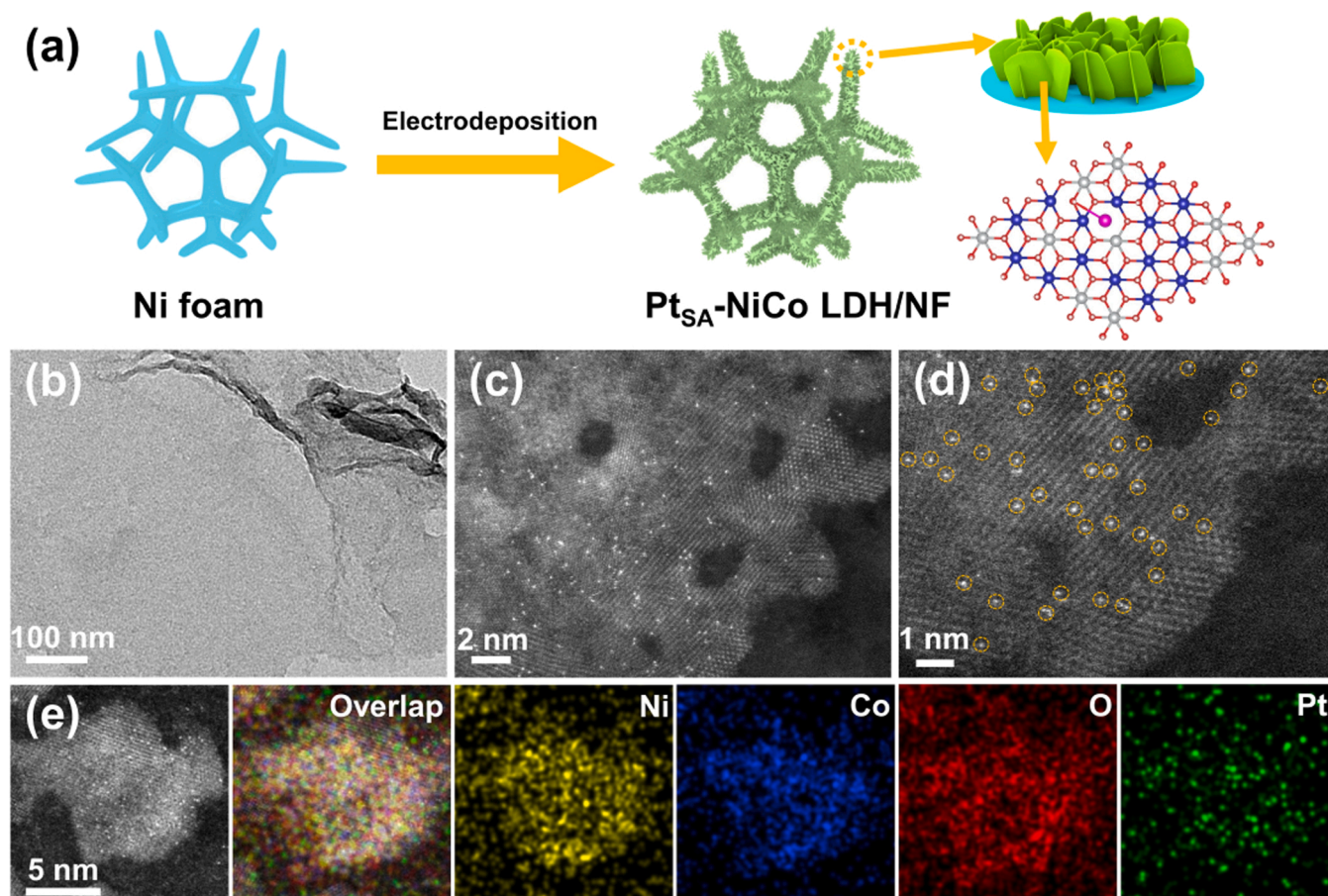
Fig. 1. (a) Schematic illustration for the fabrication of Pt_SA-NiCo LDH/NF. (b) TEM image, (c, d) Aberration-corrected HAADF-STEM images of Pt_SA-NiCo LDH/NF. (e) Aberration-corrected HAADF-STEM image and corresponding EDX element mapping images of Pt_SA-NiCo LDH/NF.
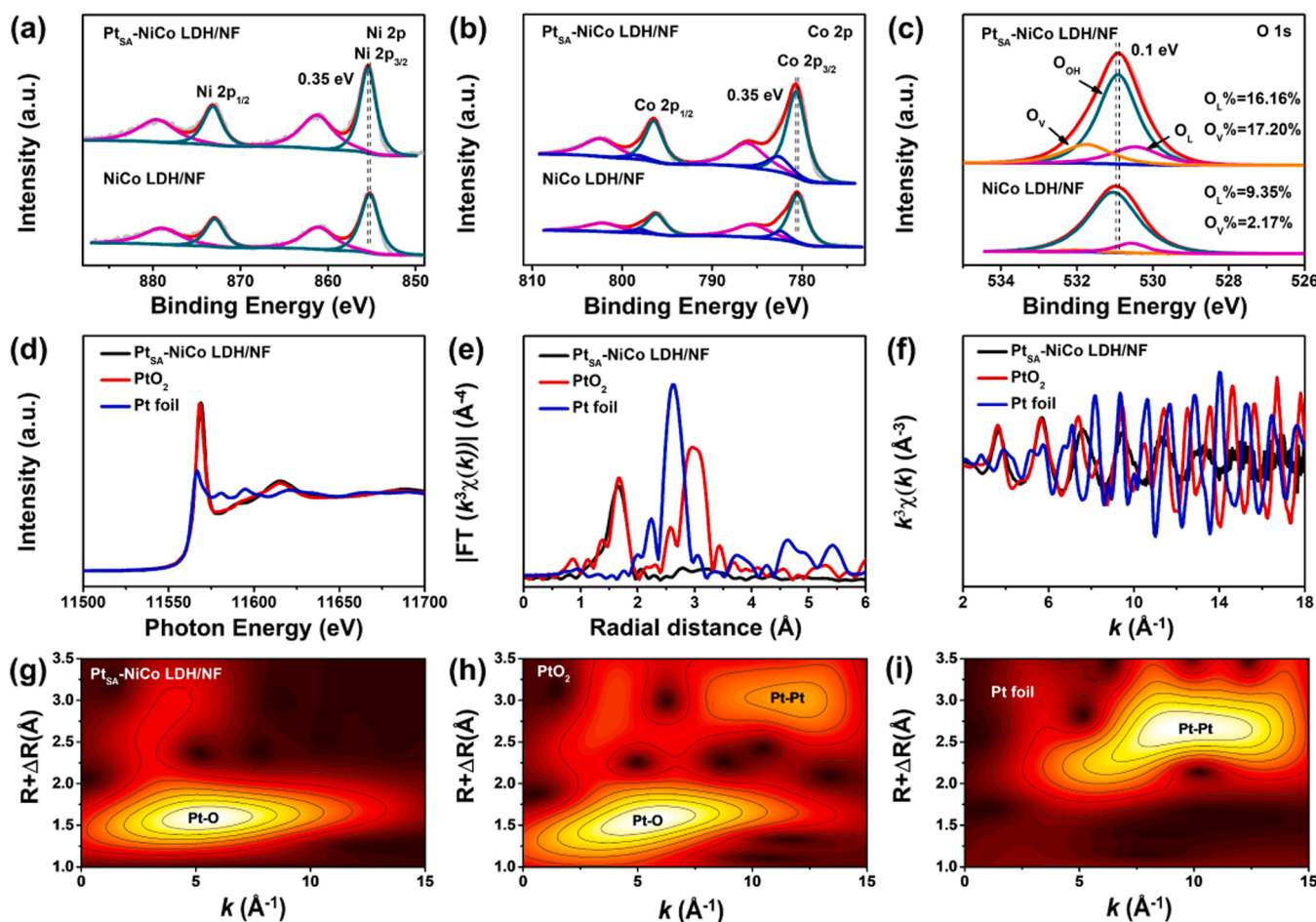
Fig. 2. XPS spectra of Ni 2p (a), Co 2p (b), and O 1 s (c) for Pt$_{SA}$-NiCo LDH/NF and NiCo LDH/NF. (d) XANES spectra, (e) EXAFS spectra in R-space, and (f) EXAFS spectra in k-space for Pt$_{SA}$-NiCo LDH/NF, PtO$_2$, and Pt foil. The EXAFS wavelet transform plots of Pt$_{SA}$-NiCo LDH/NF (g), PtO$_2$(h), and Pt foil (i).

The Co species were found to be in the valances of $+ 2$ and $+ 3$ oxidation states according to the high-resolution Co 2p spectrum in Fig. 2b[52,53]. As seen, Ni and Co in Pt$_{SA}$-NiCo LDH/NF had slight positive shifts of 0.35 and 0.35 eV compared to that of NiCo LDH/NF, and O had slight negative shifts of 0.1 eV (Fig. 2a-c), which confirmed the Pt single atoms had a strong influence on the electronic state of surrounding Ni, Co, and O atoms. The corresponding Pt 4 f peaks at 72.8 and 76.2 eV in Pt$_{SA}$--NiCo LDH/NF (Fig. S6) were assigned to Pt 4 f$_{7/2}$ and Pt 4 f$_{5/2}$ of Pt-O species [54]. Then, we performed a detailed analysis of Co species and O species. The ratio of Co^{3+}/Co^{2+} on the Pt$_{SA}$-NiCo LDH/NF (Co^{3+}/Co^{2+}=4.80) was lower than that of NiCo LDH/NF (Co^{3+}/Co^{2+}=6.59), suggesting the reduced valence state of Co and the introducing of more oxygen vacancies on the system after introduction of Pt, which could be further confirmed by the fine-scanned O 1 s XPS spectra (Fig. 2b). As can be seen, the concentration of oxygen vacancies in Pt$_{SA}$-NiCo LDH/NF was higher than NiCo LDH/NF (Fig. 2c), which is the former Co valance-reducing result. The increased surface oxygen vacancy content was balanced by the conversion of Co^{3+} to Co^{2+}. Later, the specific concentration of oxygen vacancies can be obtained from the high-resolution O1s XPS spectra. The above XPS results confirmed that the Pt single atoms can efficiently modulate the electrocatalyst's electronic structure, which was positive for the HER process. To further identify the oxygen vacancy variation of the samples, the electron paramagnetic resonance (EPR) spectrum in Fig. S7 was conducted to analyze the concentration of oxygen vacancies (g=2.004) qualitatively. It could be found that the oxygen vacancy of Pt$_{SA}$-NiCo LDH/NF was much higher than that of NiCo LDH/NF when Pt species was introduced (Fig. S1c and Fig. S2c). This also confirmed that the introduction of Pt

species led to an increase in oxygen vacancies. This means that the oxygen vacancy concentration of Pt$_{SA}$-NiCo LDH/NF can be controlled by adjusting the amount of Pt.

To further verify that Pt elements were dispersed as single atoms and study the chemical states and coordination structures of Pt species in Pt$_{SA}$-NiCo LDH/NF, we performed X-ray absorption near-edge structure (XANES) and extended X-ray absorption fine structure (EXAFS) spectrometry. The white-line intensity of Pt$_{SA}$-NiCo LDH/NF showed in XANES spectra (Fig. 2d) close to PtO$_2$, inferring the valence state of Pt in Pt$_{SA}$-NiCo LDH/NF was about $+ 4$. The salient peak at 1.66 Å of Pt$_{SA}$-NiCo LDH/NF was demonstrated by the Fourier transform of the phase-uncorrected EXAFS spectra (Fig. 2e and Fig. S8a), belonging to Pt-O coordination. Meanwhile, no Pt-Pt (2.62 Å) coordination of Pt$_{SA}$-NiCo LDH/NF was observed. According to the curve-fitting result of quantitative EXAFS, the coordination of Pt-O bonding for Pt$_{SA}$-NiCo LDH/NF is 5.3 (Fig. 2f, Fig. S8b, and Table S1). Due to the presence of unsaturated coordination of Pt and O, the catalyst will also possess stronger hydrogen evolution reaction (HER) activity. Furthermore, the Wavelet Transform analysis detected the Pt-O binding but not the Pt-Pt binding of Pt$_{SA}$-NiCo LDH/NF (Fig. 2g-i). These results not only further confirm the existence of atomic Pt in Pt$_{SA}$-NiCo LDH/NF structures but also demonstrate that O atoms act as anchor sites to combine with Pt single atoms to form Pt-O$_5$ coordination and generate strong metal-carrier interactions.

3.2. Electrochemical performances for HER

Afterward, the catalytic performance of Pt$_{SA}$-NiCo LDH/NF for HER

was measured by a three-electrode system in a 1.0 M KOH electrolyte. For comparison, the NiCo LDH/NF, Pt/C (20 wt%), and bare Ni foam were chosen as the contrast catalysts. The measured HER polarization curves showed that Pt_{SA}-NiCo LDH/NF had the lowest overpotential than contrast catalysts (Fig. 3a). Due to the introduction of Pt species, the Pt_{SA}-NiCo LDH/NF requires an overpotential of only 63 mV to provide a current density of 100 mA cm^{-2}, which was much lower than that of NiCo LDH/NF. The overpotential comparison at the current density of 10 mA cm^{-2}, 50 mA cm^{-2}, and 100 mA cm^{-2} over Pt_{SA}-NiCo LDH/NF and contrast catalysts were shown in Fig. 3b. Meanwhile, the Tafel slope is a vital parameter to evaluate the HER kinetic process of the catalyst. We calculate the Tafel slopes for each sample, the obtained Tafel slopes at low overpotentials are 50.2 mV dec^{-1}, 63.2 mV dec^{-1}, 101.8 mV dec^{-1}, and 129.2 mV dec^{-1} for Pt_{SA}-NiCo LDH/NF, Pt/C, NiCo LDH/NF, and bare Ni foam, respectively (Fig. 3c). This also validates the faster electron-transfer kinetics of Pt_{SA}-NiCo LDH/NF during HER. Since the Tafel slope is between the eigenvalues of the Volmer step (120 mV dec^{-1}) and the Heyrovsky step (40 mV dec^{-1}), it indicates that the Pt_{SA}-NiCo LDH/NF follows the Volmer-Heyrovsky mechanism in the HER[55, 56]. Moreover, the Volmer step is a rate-determining reaction. The underlying reaction mechanism illustration of electrocatalytic HER was shown in Fig. 3d. The Nyquist plots in Fig. S9 revealed the R_{ct} of Pt_{SA}-NiCo LDH/NF was significantly lower than NiCo LDH/NF and bare Ni foam, revealing that Pt_{SA}-NiCo LDH/NF can facilitate electron transfer at the electrocatalytic interface. The ECSAs of HER are reflected by the C_{dl} at the solid-liquid interface, which is investigated by cyclic voltammetry measurements in the range of 0.9–1.0 V (Fig. S10). As

expected, Pt_{SA}-NiCo LDH/NF exhibited a higher C_{dl} value than NiCo LDH/NF, which indicates a larger catalytic activity area of Pt_{SA}-NiCo LDH/NF. Next, the catalytic stability and durability for HER over Pt_{SA}-NiCo LDH/NF were evaluated by 10,000-cycle accelerated aging CV tests and the V-t test. As displayed in Fig. 3e, the LSV curve after 10, 000-cycle CV tests nearly overlaps with the primary one. The durability test result of Pt_{SA}-NiCo LDH/NF at 10 mA cm^{-2} for 50 h indicated excellent electrocatalyst durability (Fig. 3f).

3.3. Electrochemical performances for GOR

Since OER is a four-electron-proton coupling reaction, the slow kinetic process makes the oxygen evolution overpotential much higher than the theoretical water decomposition voltage (1.23 V) and the bulk of the electrical energy is consumed by the OER half-reaction. The theoretical oxidation potential of glycerol (0.003 V vs RHE) is significantly lower than OER (1.23 V vs RHE). To reduce the cell voltage of water splitting, we constructed a hybrid water electrolysis system by replacing the OER with the thermodynamically advantageous glycerol oxidation reaction (GOR). As shown in Fig. 3g, we tested the LSV curves of Pt_{SA}-NiCo LDH/NF in electrolytes with and without glycerol to determine the effect of glycerol on the HER performance of Pt_{SA}-NiCo LDH/NF. From the results, glycerol does not affect the HER performance of Pt_{SA}-NiCo LDH/NF. Therefore, we measured the remaining electrochemical performance in an electrolyte containing 1 M KOH and 0.1 M glycerol.

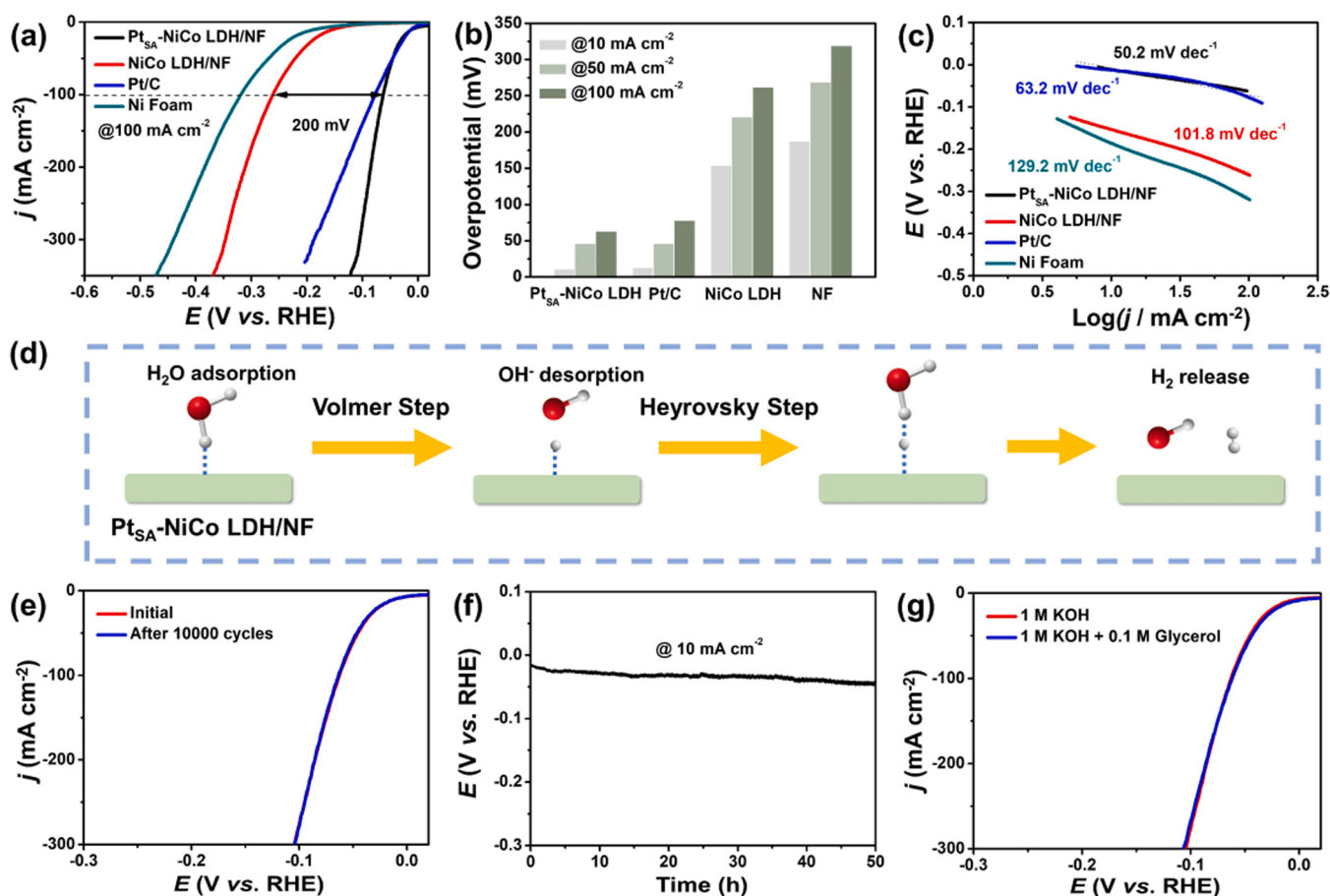Then, we compared the LSV curves of GOR and OER, and it can be

Fig. 3. (a) HER polarization curves, (b) the comparison overpotential of 10 mA cm^{-2}, 50 mA cm^{-2}, and 100 mA cm^{-2}, (c) Tafel slopes, (d) the reaction mechanism illustration of electrocatalytic HER. (e) The comparison of HER polarization curves of Pt_{SA}-NiCo LDH/NF before and after a durability test. (f) Chronopotentiometry curve for Pt_{SA}-NiCo LDH/NF with the current density of 10 mA cm^{-2} for 50 h. (g) The comparison of HER polarization curves of Pt_{SA}-NiCo LDH/NF with and without adding 0.1 M glycerol.

found that GOR possesses a lower onset potential due to the occurrence of a glycerol oxidation reaction (Fig. 4a). Specifically, Pt$_{SA}$-NiCo LDH/NF requires a potential of only 1.298 V in the glycerol-containing electrolyte to provide a current density of 100 mA cm^{-2} which is 270 mV less than the OER (Fig. 4a). And Pt$_{SA}$-NiCo LDH/NF also possesses a better reaction kinetic process in GOR in terms of the corresponding Tafel slope (Fig. 4b). In addition, we found that the introduction of Pt also promoted the glycerol oxidation reaction (Fig. S11a). Meanwhile, the conductive substrate Ni foam did not exhibit any GOR performance, which also indicates that the GOR performance of Pt$_{SA}$-NiCo LDH/NF is derived from the Pt$_{SA}$-NiCo LDH grown on Ni foam. The potentials of the catalysts at various current densities are shown in Fig. S11b. Considering that GOR is not easy to occur at low potentials and that there is an OER competition reaction at high potentials, we chose a potential window of 1.25–1.45 V for performance testing based on the LSV curves. To study the products of glycerol selective oxidation, we selected different

potentials and performed i-t tests for 12 h. By comparing the ^{1}H NMR spectra of the electrolyte before and after the reaction, and the standard HCOOH, it was found that glycerol was selectively oxidized to HCOOH accompanied by a small amount of glycerol residue (Fig. 4c). Fig. 4d revealed that the highest glycerol conversion (85%) and Faraday efficiency of formate (88.7%) were achieved at 1.375 V. To further understand the reaction products, ^{13}C NMR spectroscopy was performed. As can be seen from Fig. 4e, in addition to formate, there is a small amount of carbonate in the product. We believe this is due to the oxidation of glycerol to formate, which in turn is oxidized to carbon dioxide. Based on the above experimental results, we hypothesized the oxidation process of glycerol (Fig. 4f) [57,58]. Glycerol is first oxidized to glycerate, which then undergoes a C-C bond break to form formate and glycolate. Then, glycolate continues to be oxidized to form the main product formate. At the same time, a small amount of formate will be oxidized to form the by-product carbon dioxide. The Nyquist plots in
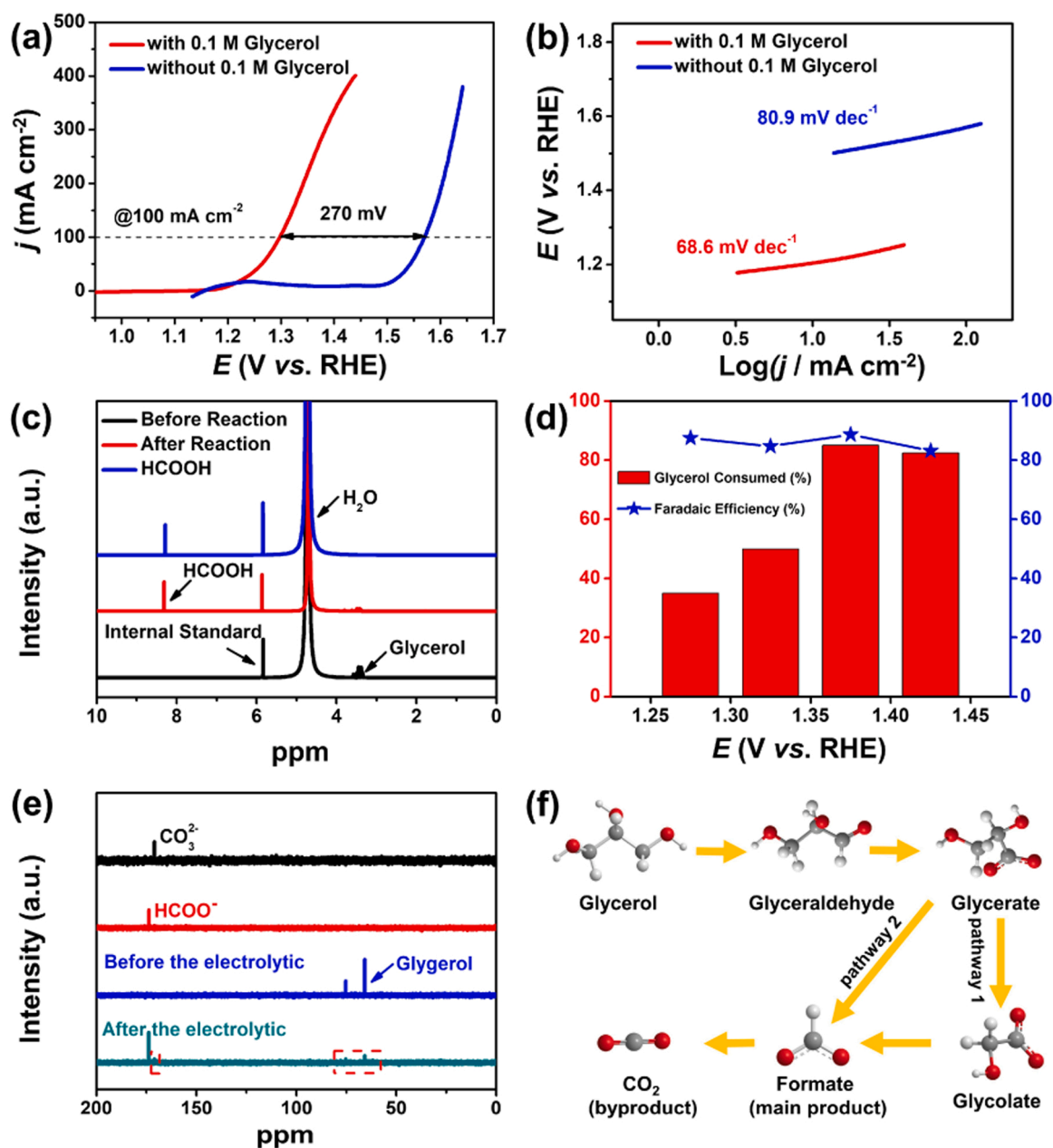
Fig. 4. (a) Comparison of GOR and OER polarization curves for Pt$_{SA}$-NiCo LDH/NF. (b) Corresponding Tafel slope for GOR and OER. (c) The ^{1}H NMR spectra of the electrolyte before and after the reaction, and the standard HCOOH. (d) The glycerol conversion and Faraday efficiency of formic acid at selected potentials. (e) The ^{13}C NMR spectra of the electrolyte before and after the reaction, CO$_3^{2-}$, and the standard HCOOH. (f) The oxidation process of glycerol.

Fig. S12 revealed the R_{ct} of Pt_{SA}-NiCo LDH/NF was significantly lower than NiCo LDH/NF and bare Ni foam, revealing that Pt_{SA}-NiCo LDH/NF can facilitate electron transfer at the electrocatalytic interface.

3.4. Electrochemical performances for HER//GOR

Based on the performance tests of the two half-reactions, we constructed a two-electrode electrolysis system with Pt_{SA}-NiCo LDH/NF both as cathode and anode electrodes, using 1 M KOH and 0.1 M glycerol as the electrolyte (Fig. 5a). The LSV curves show that the coupling of HER and GOR greatly improved cell voltage compared to conventional electrolytic water (Fig. 5b). The stability of the HER//GOR coupling system was then tested. We tested the Faraday efficiency of the cathodic hydrogen evolution reaction, and the results showed that the Faraday efficiency was close to 100% (Fig. 5c). In addition, we tested the glycerol conversion of the HER//GOR two-electrode electrolysis system. The glycerol conversion was 83.4% when the cell voltage was 1.47 V. For the formate in the electrolyte after the electrolysis reaction, we can acidify the electrolyte with formic acid, and then the resulting solution can be converted to a solid product by concentration and crystallization. The overall current density showed a stable state after this repeated test for 24 h, which also indicates that the coupled reaction system constructed by Pt_{SA}-NiCo LDH/NF is of excellent catalytic stability and durability (Fig. 5d). In addition, the morphology of Pt_{SA}-NiCo LDH/NF after the durable test was not significantly different from the original material (Fig. S13).

3.5. DFT Calculations

To gain more insight into the intrinsic relationship between catalyst structure and HER reaction activity, we simulated the atomic structure models of Pt_{SA}-NiCo LDH/NF and NiCo LDH/NF using density functional theory (DFT) (Fig. S14). As shown in Fig. S15, the charge density differences and Barder charges show that electronic interaction between Pt and NiCo LDH occurs after the introduction of the Pt single atom, as evidenced by the gain of 0.555 electrons by Pt and the loss of 0.555 electrons by NiCo LDH/NF. Such an electron interaction leads to an improvement of the charge density around the Pt single atom, a redistribution of the charge density of Pt_{SA}-NiCo LDH/NF, and optimization of the electronic structure, thus enhancing the HER performance of the catalyst. The *d*-band center is a key factor in determining the HER activity of the catalyst. Here, the relationship between the *d*-band center and the intrinsic catalytic activity is investigated by calculating the partial density of states (PDOS). The PDOS shows that the *d*-band center of Pt_{SA}-NiCo LDH/NF (−1.7088 eV) is far from the Fermi energy level than that of NiCo LDH/NF (−1.4251 eV) (Fig. 6a), indicating that the Pt atom is more capable of trapping electrons, which facilitates the reduction of H^+, thus enhancing the HER activity of Pt_{SA}-NiCo LDH/NF. Specifically, NiCo LDH as the active site catalyzes H-OH cleavage and promotes the dissociation of H_2O during the HER process, while Pt single atom as the binding site for H intermediates promotes the release of H_2 molecules. Meanwhile, Pt-O bonding accelerates proton-electron coupling and promotes H_2 molecule production.

Then, we calculated the structural models of Pt_{SA}-NiCo LDH/NF and NiCo LDH/NF after hydrogen adsorption and the ΔG_{H*} of HER at the equilibrium potential. The calculated ΔG_{H*} for Pt_{SA}-NiCo LDH/NF was − 1.19 eV and that of NiCo LDH was 1.57 eV (Fig. 6b, Fig. S16). We believe the main reason for the poor HER performance of NiCo LDH/NF is due to the too-weak adsorption of H*. When Pt single atoms were introduced into NiCo LDH/NF, it can be seen that the adsorption energy of H by the catalyst was dramatically enhanced, resulting in an improved HER performance. However, it is worth noting that although the introduction of Pt enhances the adsorption of H* by NiCo LDH/NF, Pt_{SA}-NiCo LDH/NF does not exhibit excellent HER activity after
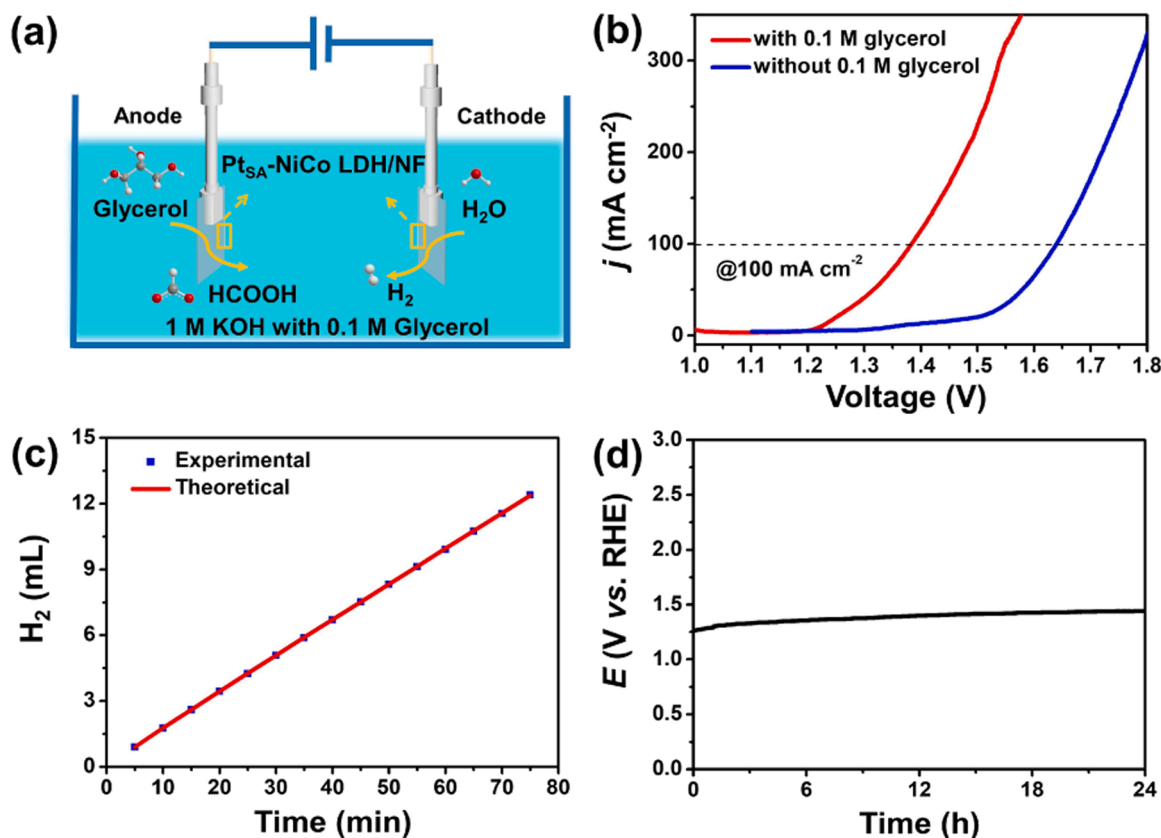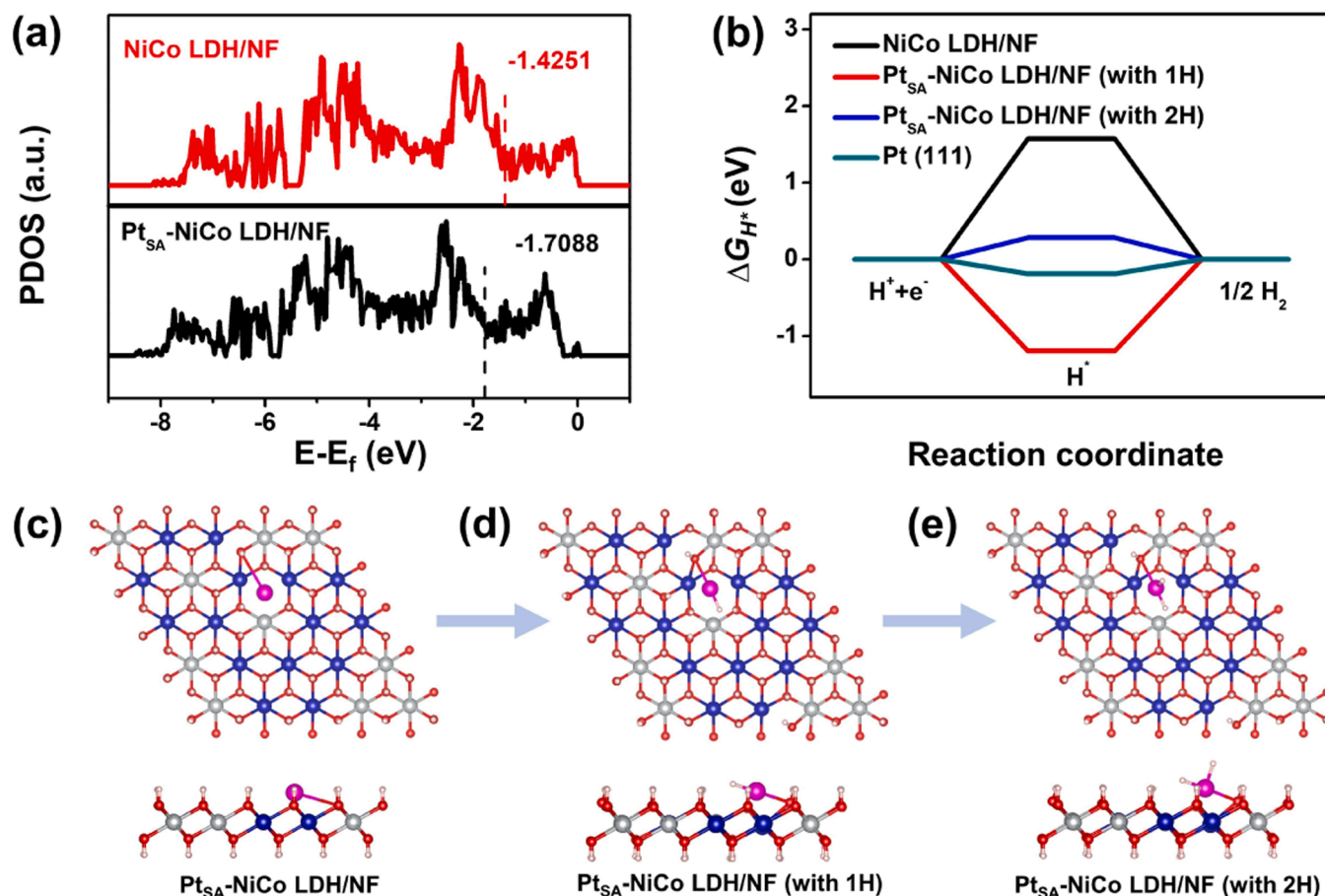

Fig. 5. (a) The schematic illustration of HER//GOR, (b) LSV curves of HER//GOR and HER//OER, (c) Faraday efficiency of HER, and (d) stability test of HER//GOR at 10 mA cm^{-2} for 24 h.

Fig. 6. (a) The PDOS patterns and the *d*-band center of Pt$_{SA}$-NiCo LDH/NF and NiCo LDH/NF. (b) The calculated ΔG_{H*} for Pt$_{SA}$-NiCo LDH (with 1 H), Pt$_{SA}$-NiCo LDH (with 2 H), NiCo LDH/NF, and Pt (111). (c-d) Pt$_{SA}$-NiCo LDH/NF structural models before and after hydrogen adsorption.

hydrogen adsorption to the poor activity of NiCo LDH/NF itself. As far as we know, the closer ΔG_{H*} is to 0, the better HER performance the catalyst can exhibit. Although the ΔG_{H*} of Pt$_{SA}$-NiCo LDH/NF is closer to 0 than that of NiCo LDH/NF, it is still too far from 0 eV.

Empirically, we believe that the first H* adsorbed by Pt$_{SA}$-NiCo LDH/NF during hydrogen evolution does not play a decisive role in promoting HER. Since the strong adsorption of Pt for H*, there is still spare space for Pt to adsorb H* when it adsorbs one H*. It is only after Pt continues to adsorb one or more H* that it causes improvement in HER performance. So, we constructed a structural model of Pt$_{SA}$-NiCo LDH/NF adsorption of two H* and calculated the change of ΔG_{H*}. The calculated ΔG_{H*} for Pt$_{SA}$-NiCo LDH/NF decreases from $-$ 1.19–0.28 eV as the H* coverage increases from 1 to 2, which is close to the ideal HER catalyst (Fig. 6b, ΔG_{H*} of Pt (111) is $-$ 0.19 eV). This result also confirmed our previous conjecture that the Pt single atom in Pt$_{SA}$-NiCo LDH/NF needs to adsorb multiple hydrogen atoms so that the hydrogen adsorption energy can be fully optimized and the kinetics of HER can be significantly improved, to finally exhibit excellent HER performance.

4. Conclusion

In summary, we constructed Pt$_{SA}$-NiCo LDH/NF by combining Pt single atoms with O atoms using oxygen vacancies in NiCo LDH as anchor sites. Among this, Pt single atoms combine with O atoms to form Pt-O$_5$ coordination and produce strong electronic interaction with LDHs. The as-obtained Pt$_{SA}$-NiCo LDHs/NF as the electrode for HER//GOR two-electrode hybrid water electrolysis system can provide a current density of 100 mA cm^{-2} at the cell voltage of 1.37 V and achieve the selective oxidation of glycerol on the anode. DFT revealed that the

introduction of Pt single atom reduced the *d*-band center. In addition, when two H is adsorbed on the surface of Pt$_{SA}$-NiCo LDHs/NF, the kinetics of HER are fully optimized, thus showing excellent HER performance. This work establishes a HER//GOR hybrid water electrolysis system efficient for energy-saving hydrogen production and selective oxidation of glycerol to formate at an anode.

CRediT authorship contribution statement

Hongjie Yu: Writing, Investigation, Formal analysis, Funding acquisition. **Wenxin Wang**: Visualization. **Qiqi Mao**: Data curation. **Kai Deng**: Visualization, Funding acquisition. **Ziqiang Wang**: Writing – review & editing, Funding acquisition. **You Xu**: Writing – review & editing, Supervision, Formal analysis. **Xiaonian Li**: Supervision. **Hongjing Wang**: Conceptualization, Supervision, Visualization, Funding acquisition. **Liang Wang:** Writing – review & editing, Supervision, Funding acquisition.

Declaration of Competing Interest

The authors declare that they have no known competing financial interests or personal relationships that could have appeared to influence the work reported in this paper.

Data Availability

Data will be made available on request.

Acknowledgements

Appendix A. Supporting information

Supplementary data associated with this article can be found in the online version at doi:10.1016/j.apcatb.2023.122617.

References

[1] J. Zhu, L. Hu, P. Zhao, L.Y.S. Lee, K.Y. Wong, Recent advances in electrocatalytic hydrogen evolution using nanoparticles, Chem. Rev. 120 (2020) 851–918l, https://doi.org/10.1021/acs.chemrev.9b00248.

[2] Z.-Y. Yu, C.-C. Lang, M.-R. Gao, Y. Chen, Q.-Q. Fu, Y. Duan, S.-H. Yu, Ni-Mo-O nanorod-derived composite catalysts for efficient alkaline water-to-hydrogen conversion via urea electrolysis, Energy Environ. Sci. 11 (2018) 1890–1897l, https://doi.org/10.1039/c8ee00521d.

[3] Y. Luo, Z. Zhang, M. Chhowalla, B. Liu, Recent advances in design of electrocatalysts for high-current-density water splitting, Adv. Mater. 34 (2022), 2108133l, https://doi.org/10.1002/adma.202108133.

[4] Z.Y. Yu, Y. Duan, X.Y. Feng, X. Yu, M.R. Gao, S.H. Yu, Clean and affordable hydrogen fuel from alkaline water splitting: past, recent progress, and future prospects, Adv. Mater. 33 (2021), 2007100l, https://doi.org/10.1002/adma.202007100.

[5] K. Deng, Q. Mao, W. Wang, P. Wang, Z. Wang, Y. Xu, X. Li, H. Wang, L. Wang, Defect-rich low-crystalline Rh metallene for efficient chlorine-free H_2 production by hydrazine-assisted seawater splitting, Appl. Catal. B: Environ. 310 (2022), 121338l, https://doi.org/10.1016/j.apcatb.2022.121338.

[6] Y. Zhang, B. Zhou, Z. Wei, W. Zhou, D. Wang, J. Tian, T. Wang, S. Zhao, J. Liu, L. Tao, S. Wang, Coupling glucose-assisted Cu(I)/Cu(II) redox with electrochemical hydrogen production, Adv. Mater. 33 (2021), 2104791l, https://doi.org/10.1002/adma.202104791.

[7] M. Jin, X. Zhang, S. Niu, Q. Wang, R. Huang, R. Ling, J. Huang, R. Shi, A. Amini, C. Cheng, Strategies for designing high-performance hydrogen evolution reaction electrocatalysts at large current densities above 1000 mA cm(-2), ACS Nano 16 (2022) 11577–11597l, https://doi.org/10.1021/acsnano.2c02820.

[8] H. Sun, W. Zhang, J.-G. Li, Z. Li, X. Ao, K.-H. Xue, K.K. Ostrikov, J. Tang, C. Wang, Rh-engineered ultrathin NiFe-LDH nanosheets enable highly-efficient overall water splitting and urea electrolysis, Appl. Catal. B: Environ. 284 (2021), 119740l, https://doi.org/10.1016/j.apcatb.2020.119740.

[9] Y. Li, X. Tan, S. Chen, X. Bo, H. Ren, S.C. Smith, C. Zhao, Processable surface modification of nickel-heteroatom (N, S) bridge sites for promoted alkaline hydrogen evolution, Angew. Chem. Int. Ed. 58 (2019) 461–466l, https://doi.org/10.1002/anie.201808629.

[10] T. Zhao, Y. Wang, S. Karuturi, K. Catchpole, Q. Zhang, C. Zhao, Design and operando/in situ characterization of precious-metal-free electrocatalysts for alkaline water splitting, Carbon Energy 2 (2020) 582–613l, https://doi.org/10.1002/cey2.79.

[11] A. Ali, P.K. Shen, Nonprecious metal's graphene-supported electrocatalysts for hydrogen evolution reaction: Fundamentals to applications, Carbon Energy 2 (2019) 99–121l, https://doi.org/10.1002/cey2.26.

[12] J. Zhang, E. Wang, S. Cui, S. Yang, X. Zou, Y. Gong, Single-atom Pt anchored on oxygen vacancy of monolayer $Ti_3C_2T_x$ for superior hydrogen evolution, Nano Lett. 22 (2022) 1398–1405l, https://doi.org/10.1021/acs.nanolett.1c04809.

[13] Q. Liang, W. Li, L. Xie, Y. He, B. Qiu, H. Zeng, S. Zhou, J. Zeng, T. Liu, M. Yan, K. Liang, O. Terasaki, L. Jiang, B. Kong, General synergistic capture-bonding superassembly of atomically dispersed catalysts on micropore-vacancy frameworks, Nano Lett. 22 (2022) 2889–2897l, https://doi.org/10.1021/acs.nanolett.2c00042.

[14] H. Sun, X. Xu, H. Kim, W. Jung, W. Zhou, Z. Shao, Electrochemical water splitting: bridging the gaps between fundamental research and industrial applications, Energy Environ. Mater. 124411 (2022), https://doi.org/10.1002/eem2.12441.

[15] H. Li, S. Wang, H. Sawada, G.G. Han, T. Samuels, C.S. Allen, A.I. Kirkland, J.C. Grossman, J.H. Warner, Atomic structure and dynamics of single platinum atom interactions with monolayer MoS_2, ACS Nano 11 (2017) 3392–3403l, https://doi.org/10.1021/acsnano.7b00796.

[16] M.D. Hossain, Z. Liu, M. Zhuang, X. Yan, G.L. Xu, C.A. Gadre, A. Tyagi, I.H. Abidi, C.J. Sun, H. Wong, A. Guda, Y. Hao, X. Pan, K. Amine, Z. Luo, Rational design of graphene-supported single atom catalysts for hydrogen evolution reaction, Adv. Energy Mater. 9 (2019), 1803689l, https://doi.org/10.1002/aenm.201803689.

[17] X. Zheng, P. Li, S. Dou, W. Sun, H. Pan, D. Wang, Y. Li, Non-carbon-supported single-atom site catalysts for electrocatalysis, Energy Environ. Sci. 14 (2021) 2809–2858l, https://doi.org/10.1039/d1ee00248a.

[18] K. Liu, J. Fu, L. Zhu, X. Zhang, H. Li, H. Liu, J. Hu, M. Liu, Single-atom transition metals supported on black phosphorene for electrochemical nitrogen reduction, Nanoscale 12 (2020) 4903–4908l, https://doi.org/10.1039/c9nr09117c.

[19] Z. Zhang, C. Feng, C. Liu, M. Zuo, L. Qin, X. Yan, Y. Xing, H. Li, R. Si, S. Zhou, J. Zeng, Electrochemical deposition as a universal route for fabricating single-atom catalysts, Nat. Commun. 11 (2020) 1215l, https://doi.org/10.1038/s41467-020-14917-6.

[20] S. Ye, F. Luo, Q. Zhang, P. Zhang, T. Xu, Q. Wang, D. He, L. Guo, Y. Zhang, C. He, X. Ouyang, M. Gu, J. Liu, X. Sun, Highly stable single Pt atomic sites anchored on aniline-stacked graphene for hydrogen evolution reaction, Energy Environ. Sci. 12 (2019) 1000–1007l, https://doi.org/10.1039/c8ee02888e.

[21] Q. Yang, H. Liu, P. Yuan, Y. Jia, L. Zhuang, H. Zhang, X. Yan, G. Liu, Y. Zhao, J. Liu, S. Wei, L. Song, Q. Wu, B. Ge, L. Zhang, K. Wang, X. Wang, C.R. Chang, X. Yao, Single carbon vacancy traps atomic platinum for hydrogen evolution catalysis, J. Am. Chem. Soc. 144 (2022) 2171–2178l, https://doi.org/10.1021/jacs.1c10814.

[22] C. Wang, K. Wang, Y. Feng, C. Li, X. Zhou, L. Gan, Y. Feng, H. Zhou, B. Zhang, X. Qu, H. Li, J. Li, A. Li, Y. Sun, S. Zhang, G. Wang, Y. Guo, S. Yang, T. Zhou, F. Dong, K. Zheng, L. Wang, J. Huang, Z. Zhang, X. Han, Co and Pt dual-single-atoms with oxygen-coordinated Co-O-Pt dimer sites for ultrahigh photocatalytic hydrogen evolution efficiency, Adv. Mater. 33 (2021), 2003327l, https://doi.org/10.1002/adma.202003327.

[23] R. Pan, R. Lin, Y. Chen, S. Liu, W. Zhu, X. Cao, W. Chen, K. Wu, W.-C. Cheong, Y. Wang, L. Zheng, J. Luo, Y. Lin, Y. Liu, C. Liu, J. Li, Q. Lu, X. Chen, D. Wang, Q. Peng, C. Chen, Y. Li, Design of single-atom Co-N_5 catalytic site: a robust electrocatalyst for CO_2 reduction with nearly 100% CO selectivity and remarkable stability, J. Am. Chem. Soc. 140 (2018) 4218–4221l, https://doi.org/10.1021/jacs.8b00814.

[24] W. Guo, Z. Wang, X. Wang, Y. Wu, General design concept for single-atom catalysts toward heterogeneous catalysis, Adv. Mater. 33 (2021), 2004287l, https://doi.org/10.1002/adma.202004287.

[25] B. Hu, K. Sun, Z. Zhuang, Z. Chen, S. Liu, W.C. Cheong, C. Chen, M. Hu, X. Cao, J. Ma, R. Tu, X. Zheng, H. Xiao, X. Chen, Y. Cui, Q. Peng, C. Chen, Y. Li, Distinct crystal-facet-dependent behaviors for single-atom palladium-on-ceria catalysts: enhanced stabilization and catalytic properties, Adv. Mater. 34 (2022), 2107721l, https://doi.org/10.1002/adma.202107721.

[26] J. Zhang, J. Liu, L. Xi, Y. Yu, N. Chen, S. Sun, W. Wang, K.M. Lange, B. Zhang, Single-atom Au/NiFe layered double hydroxide electrocatalyst: probing the origin of activity for oxygen evolution reaction, J. Am. Chem. Soc. 140 (2018) 3876–3879l, https://doi.org/10.1021/jacs.8b00752.

[27] M. Asnavandi, Y. Yin, Y. Li, C. Sun, C. Zhao, Promoting oxygen evolution reactions through introduction of oxygen vacancies to benchmark NiFe-OOH catalysts, ACS Energy Lett. 3 (2018) 1515–1520l, https://doi.org/10.1021/acsenergylett.8b00696.

[28] J. Li, L. Wang, H. He, Y. Chen, Z. Gao, N. Ma, B. Wang, L. Zheng, R. Li, Y. Wei, J. Xu, Y. Xu, B. Cheng, Z. Yin, D. Ma, Interface construction of NiCo LDH/NiCoS based on the 2D ultrathin nanosheet towards oxygen evolution reaction, Nano Res 15 (2022) 4986–4995l, https://doi.org/10.1007/s12274-022-4144-6.

[29] Q. He, S. Qiao, Q. Zhou, Y. Zhou, H. Shou, P. Zhang, W. Xu, D. Liu, S. Chen, X. Wu, L. Song, Confining high-valence iridium single sites onto nickel oxyhydroxide for robust oxygen evolution, Nano Lett. 22 (2022) 3832–3839l, https://doi.org/10.1021/acs.nanolett.2c01124.

[30] Y. Zhao, P.V. Kumar, X. Tan, X. Lu, X. Zhu, J. Jiang, J. Pan, S. Xi, H.Y. Yang, Z. Ma, T. Wan, D. Chu, W. Jiang, S.C. Smith, R. Amal, Z. Han, X. Lu, Modulating Pt-O-Pt atomic clusters with isolated cobalt atoms for enhanced hydrogen evolution catalysis, Nat. Commun. 13 (2022) 2430l, https://doi.org/10.1038/s41467-022-30155-4.

[31] F.Y. Yu, Z.L. Lang, L.Y. Yin, K. Feng, Y.J. Xia, H.Q. Tan, H.T. Zhu, J. Zhong, Z.H. Kang, Y.G. Li, Pt-O bond as an active site superior to Pt(0) in hydrogen evolution reaction, Nat. Commun. 11 (2020) 490l, https://doi.org/10.1038/s41467-019-14274-z.

[32] K.L. Zhou, Z. Wang, C.B. Han, X. Ke, C. Wang, Y. Jin, Q. Zhang, J. Liu, H. Wang, H. Yan, Platinum single-atom catalyst coupled with transition metal/metal oxide heterostructure for accelerating alkaline hydrogen evolution reaction, Nat. Commun. 12 (2021) 3783l, https://doi.org/10.1038/s41467-021-24079-8.

[33] Y. Huang, X. Chong, C. Liu, Y. Liang, B. Zhang, Boosting hydrogen production by anodic oxidation of primary amines over a NiSe nanorod electrode, Angew. Chem. Int. Ed. 57 (2018) 13163–13166l, https://doi.org/10.1002/anie.201807717.

[34] Y. Li, Y. Zhao, F.M. Li, Z. Dang, P. Gao, Ultrathin NiSe nanosheets on ni foam for efficient and durable hydrazine-assisted electrolytic hydrogen production, ACS Appl. Mater. Interfaces 13 (2021) 34457–34467l, https://doi.org/10.1021/acsami.1c09503.

[35] Z. Wang, L. Xu, F. Huang, L. Qu, J. Li, K.A. Owusu, Z. Liu, Z. Lin, B. Xiang, X. Liu, K. Zhao, X. Liao, W. Yang, Y.B. Cheng, L. Mai, Copper-nickel nitride nanosheets as efficient bifunctional catalysts for hydrazine-assisted electrolytic hydrogen production, Adv. Energy Mater. 9 (2019), 1900390l, https://doi.org/10.1002/aenm.201900390.

[36] Q. Mao, K. Deng, H. Yu, Y. Xu, Z. Wang, X. Li, L. Wang, H. Wang, In situ reconstruction of partially hydroxylated porous Rh metallene for ethylene glycol-assisted seawater splitting, Adv. Funct. Mater. 32 (2022), 2201081l, https://doi.org/10.1002/adfm.202201081.

[37] J.Y. Zhang, H. Wang, Y. Tian, Y. Yan, Q. Xue, T. He, H. Liu, C. Wang, Y. Chen, B.Y. Xia, Anodic hydrazine oxidation assists energy-efficient hydrogen evolution over a bifunctional cobalt perselenide nanosheet electrode, Angew. Chem. Int. Ed. 57 (2018) 7649–7653l.

[38] T. Wang, X. Cao, L. Jiao, Progress in hydrogen production coupled with electrochemical oxidation of small molecules, Angew. Chem. Int. Ed. (2022), https://doi.org/10.1002/anie.202213328.

[39] M. Zhang, J. Guan, Y. Tu, S. Chen, Y. Wang, S. Wang, L. Yu, C. Ma, D. Deng, X. Bao, Highly efficient H_2 production from H_2S via a robust graphene-encapsulated metal

catalyst, Energy Environ. Sci. 13 (2020) 119–126l, https://doi.org/10.1039/c9ee03231b.

[40] Y. Xu, M. Liu, S. Wang, K. Ren, M. Wang, Z. Wang, X. Li, L. Wang, H. Wang, Integrating electrocatalytic hydrogen generation with selective oxidation of glycerol to formate over bifunctional nitrogen-doped carbon coated nickel-molybdenum-nitrogen nanowire arrays, Appl. Catal. B: Environ. 298 (2021), 120493l, https://doi.org/10.1016/j.apcatb.2021.120493.

[41] Y. Xu, T. Liu, K. Shi, H. Yu, K. Deng, Z. Wang, X. Li, L. Wang, H. Wang, Iridium-incorporated Co(3)O(4) with lattice expansion for energy-efficient green hydrogen production coupled with glycerol valorization, Chem. Commun. 59 (2023) 1817–1820l, https://doi.org/10.1039/d2cc06931h.

[42] Y. Li, X. Wei, L. Chen, J. Shi, M. He, Nickel-molybdenum nitride nanoplate electrocatalysts for concurrent electrolytic hydrogen and formate productions, Nat. Commun. 10 (2019) 5335l, https://doi.org/10.1038/s41467-019-13375-z.

[43] J. Hao, J. Liu, D. Wu, M. Chen, Y. Liang, Q. Wang, L. Wang, X.-Z. Fu, J.-L. Luo, In situ facile fabrication of Ni(OH)2 nanosheet arrays for electrocatalytic co-production of formate and hydrogen from methanol in alkaline solution, Appl. Catal. B: Environ. 281 (2021), 119510l, https://doi.org/10.1016/j.apcatb.2020.119510.

[44] Y. Xu, M. Liu, M. Wang, T. Ren, K. Ren, Z. Wang, X. Li, L. Wang, H. Wang, Methanol electroreforming coupled to green hydrogen production over bifunctional NiIr-based metal-organic framework nanosheet arrays, Appl. Catal. B: Environ. 300 (2022), 120753l, https://doi.org/10.1016/j.apcatb.2021.120753.

[45] Y. Yang, T. Mu, Electrochemical oxidation of biomass derived 5-hydroxymethyl-furfural (HMF): pathway, mechanism, catalysts and coupling reactions, Green. Chem. 23 (2021) 4228–4254l, https://doi.org/10.1039/d1gc00914a.

[46] Y. Song, Z. Li, K. Fan, Z. Ren, W. Xie, Y. Yang, M. Shao, M. Wei, Ultrathin layered double hydroxides nanosheets array towards efficient electrooxidation of 5-hydroxymethylfurfural coupled with hydrogen generation, Appl. Catal. B: Environ. 299 (2021), 120669l, https://doi.org/10.1016/j.apcatb.2021.120669.

[47] H. Sun, L. Li, Y. Chen, H. Kim, X. Xu, D. Guan, Z. Hu, L. Zhang, Z. Shao, W. Jung, Boosting ethanol oxidation by NiOOH-CuO nano-heterostructure for energy-saving hydrogen production and biomass upgrading, Appl. Catal. B: Environ. 325 (2023), 122388l, https://doi.org/10.1016/j.apcatb.2023.122388.

[48] Z. Zou, L. Wu, F. Yang, C. Cao, Q. Meng, J. Luo, W. Zhou, Z. Tong, J. Chen, S. Chen, S. Zhou, J. Wang, S. Deng, Delicate tuning of the Ni/Co ratio in bimetal layered double hydroxides for efficient N(2) electroreduction, ChemSusChem 15 (2022), 202200127l, https://doi.org/10.1002/cssc.202200127.

[49] H. Tian, K. Zhu, Y. Jiang, L. Wang, W. Li, Z. Yu, C. Wu, Heterogeneous assembly of Ni-Co layered double hydroxide/sulfonated graphene nanosheet composites as battery-type materials for hybrid supercapacitors, Nanoscale Adv. 3 (2021) 2924–2933l, https://doi.org/10.1039/d1na00001b.

[50] H. You, D. Wu, D. Si, M. Cao, F. Sun, H. Zhang, H. Wang, T.F. Liu, R. Cao, Monolayer NiIr-layered double hydroxide as a long-lived efficient oxygen evolution catalyst for seawater splitting, J. Am. Chem. Soc. 144 (2022) 9254–9263l, https://doi.org/10.1021/jacs.2c00242.

[51] J. Xu, I. Amorim, Y. Li, J. Li, Z. Yu, B. Zhang, A. Araujo, N. Zhang, L. Liu, Stable overall water splitting in an asymmetric acid/alkaline electrolyzer comprising a bipolar membrane sandwiched by bifunctional cobalt-nickel phosphide nanowire electrodes, Carbon Energy 2 (2020) 646–655l, https://doi.org/10.1002/cey2.56.

[52] Q. Li, F. Huang, S. Li, H. Zhang, X.Y. Yu, Oxygen Vacancy Engineering Synergistic with Surface Hydrophilicity Modification of Hollow Ru Doped CoNi-LDH Nanotube Arrays for Boosting Hydrogen Evolution, Small 18 (2022), 2104323l, https://doi.org/10.1002/smll.202104323.

[53] J. Chen, H. Zhang, J. Yu, D. Guan, S. She, W. Zhou, Z. Shao, Self-catalyzed formation of strongly interconnected multiphase molybdenum-based composites for efficient hydrogen evolution, Carbon Energy 4 (2021) 77–87l, https://doi.org/10.1002/cey2.156.

[54] X. Lyu, J. Chen, J. Liu, Y. Peng, S. Duan, X. Ma, W. Wang, Reversing a platinum micromotor by introducing platinum oxide, Angew. Chem. Int. Ed. 61 (2022), 2022010181, https://doi.org/10.1002/anie.202201018.

[55] Y. Yan, J. Lin, T. Xu, B. Liu, K. Huang, L. Qiao, S. Liu, J. Cao, S.C. Jun, Y. Yamauchi, J. Qi, Atomic-level platinum filling into Ni-vacancies of dual-deficient NiO for boosting electrocatalytic hydrogen evolution, Adv. Energy Mater. 12 (2022), 2200434l, https://doi.org/10.1002/aenm.202200434.

[56] H. Sun, X. Xu, Y. Song, W. Zhou, Z. Shao, Designing high-valence metal sites for electrochemical water splitting, Adv. Funct. Mater. 31 (2021), 2009779l, https://doi.org/10.1002/adfm.202009779.

[57] X. Han, H. Sheng, C. Yu, T.W. Walker, G.W. Huber, J. Qiu, S. Jin, Electrocatalytic oxidation of glycerol to formic acid by CuCo2O4 spinel oxide nanostructure catalysts, ACS Catal. 10 (2020) 6741–6752l, https://doi.org/10.1021/acscatal.0c01498.

[58] X. Yu, E.C. Dos Santos, J. White, G. Salazar-Alvarez, L.G.M. Pettersson, A. Cornell, M. Johnsson, Electrocatalytic glycerol oxidation with concurrent hydrogen evolution utilizing an efficient MoOx/Pt catalyst, Small 17 (2021), 2104288l, https://doi.org/10.1002/smll.202104288.